Research Square

Preprints are preliminary reports that have not undergone peer review.
They should not be considered conclusive, used to inform clinical practice,
or referenced by the media as validated information.

Silent convergence failures in SCAPS-1D: unphysical open-circuit voltages and unflagged anomalies in temperature-dependent Perovskite Solar Cell simulations

Nahuel Martinez

nahuelm@ifas.exa.unicen.edu.ar

CIFICEN, UNCPBA-CICPBA-CONICET

Jannatul Mauya

Rajshahi University of Engineering and Technology

Martin Santiago

CIFICEN, UNCPBA-CICPBA-CONICET

Research Article

Keywords:

Posted Date: November 9th, 2026

DOI: https://doi.org/10.21203/rs.3.rs-11322113/v1

License: This work is licensed under a Creative Commons Attribution 4.0 International License.
Read Full License

Additional Declarations: No competing interests reported.

Silent convergence failures in SCAPS-1D: unphysical open-circuit voltages and unflagged anomalies in temperature-dependent Perovskite Solar Cell simulations

Authors:
Nahuel Martinez[1*]; Jannatul Mauya[2]; Martin Santiago[1]
[1] CIFICEN, UNCPBA-CICPBA-CONICET, Tandil, Buenos Aires, Argentina.
[2] Rajshahi University of Engineering and Technology, Rajshahi, Bangladesh.
*Corresponding author: Nahuel Martinez

Abstract:
Perovskite solar cells (PSCs) based on inorganic charge transport layers are attracting increasing attention for their thermal stability and low fabrication cost, yet the temperature-dependent behavior of carrier extraction in these devices remains incompletely understood. Here we show that numerical simulations using SCAPS-1D can fail silently: temperature sweeps of CuI/MAPbI3/ETL and Spiro-OMeTAD/MAPbI3/ETL architectures, performed across three electron transport layers (SnO2, TiO2, ZnO) and two absorber thicknesses (100 nm and 500 nm) over the range 250–350 K, reveal two distinct convergence failure modes, neither of which is reliably flagged by the solver. In one, open-circuit voltage (Voc) and fill factor (FF) become unresolvable while a seemingly ordinary short-circuit current density (Jsc) is still returned. In the other - observed exclusively in Spiro-OMeTAD-based configurations - the solver returns a Voc that exceeds the thermodynamic ceiling Eg/q by up to 2.9×, with no indication that the output is physically impossible. Three candidate mechanisms for the first failure mode - Debye length confinement breakdown, conduction band offset inversion, and extrinsic-to-intrinsic carrier transition - were analytically ruled out. We demonstrate instead that it is caused by thermally activated divergence of the series resistance Rs at the ETL/perovskite interface: Rs increases by two to four orders of magnitude at anomaly onset, following Arrhenius behavior (R^2 = 0.88–0.99) with activation energies of 0.59–0.87 eV consistent with thermionic emission across the conduction band spike ΔEc. Both failure modes are ETL/HTL-specific and perovskite thickness-independent - identical patterns at 100 nm and 500 nm confirm an interfacial rather than bulk origin. While this study covers a limited set of architectures, the central implication is general: convergence anomalies in temperature-dependent SCAPS-1D simulations do not always announce themselves, and physically invalid or incomplete results may have gone unnoticed in prior work. These results provide a physically grounded framework for identifying such failures and establish ETL conduction band alignment and HTL identity as key design parameters governing extraction stability and Voc validity, respectively.

Introduction:

Perovskite solar cells (PSCs) have emerged as one of the most promising photovoltaic technologies of the past decade, with power conversion efficiencies surpassing 25% in certified laboratory devices and an unmatched combination of tunable bandgap, low-temperature processability, and low material cost.[1–3] The archetypal absorber methylammonium lead iodide ($MAPbI_3$), with a direct bandgap of

approximately 1.51 eV and high absorption coefficient across the visible spectrum, remains as a widely studied composition for fundamental device physics investigations.[3,4] Central to PSC performance are the charge-selective transport layers flanking the absorber: the hole transport layer (HTL), which extracts photogenerated holes, and the electron transport layer (ETL), which collects electrons. The choice and properties of these layers critically determine interfacial recombination, charge extraction efficiency, and ultimately device stability under operating conditions.[5]

Among hole transport materials, Spiro-OMeTAD has long served as the organic reference owing to its favorable band alignment with $MAPbI_3$ and high hole mobility. However, its thermal instability, hygroscopicity, and high synthesis cost have motivated extensive investigation of inorganic alternatives. Copper(I) iodide (CuI) has attracted particular interest as an HTL candidate: it offers a wide bandgap (≈2.98 eV), high intrinsic hole mobility (≈40 $cm^2\ V^{-1}\ s^{-1}$), chemical stability, and straightforward deposition from solution.[6] On the electron-collecting side, tin dioxide (SnO_2) has largely displaced TiO_2 as the preferred ETL in high-efficiency architectures owing to its wider bandgap, higher electron mobility, and compatibility with low-temperature processing;[5,7] ZnO and TiO_2 remain actively studied alternatives with distinct band alignments and transport properties.[8]

Understanding the thermal dependence of PSC performance is essential for reliable outdoor operation, where module temperatures routinely span 270–350 K depending on climate and encapsulant design.[9] At the device level, temperature affects carrier concentration, mobility, recombination rates, and band alignment simultaneously, producing a complex interplay that cannot be disentangled by experiment alone.[10] The general framework for temperature-dependent photovoltaic parameters - describing how V_{oc}, J_{sc}, and fill factor respond to thermal variations - was established by Green,[9] yet its application to the specific heterostructures of PSCs, where ionic migration, interfacial traps, and multiple semiconductor junctions coexist, remains an active area of investigation.[11,12] Experimental characterization of $MAPbI_3$-based devices across wide temperature ranges is further complicated by the material's known phase transitions (tetragonal-to-cubic near 327 K) and susceptibility to moisture-induced degradation above ~353 K, making controlled thermal studies technically demanding.[13]

Numerical drift-diffusion simulation using SCAPS-1D has become the standard computational tool for investigating carrier transport in PSCs, owing to its ability to model multilayer heterostructures, interface defects, and temperature-dependent parameters within a self-consistent Poisson–drift-diffusion framework.[14,15] A large and growing body of literature employs SCAPS-1D to optimize transport layer materials, thicknesses, and doping levels across a wide range of perovskite

compositions.[4,16] However, the reliability of these simulations has come under scrutiny: Saidarsan et al. (2025) analyzed over 250 SCAPS-1D-based studies and documented systematic use of non-physical input parameters - including trap densities orders of magnitude below experimental values and doping levels exceeding semiconductor stability limits - yielding efficiencies that violate the Shockley–Queisser limit.[17] This growing concern underscores the need for rigorous parameter validation and mechanistic interpretation of SCAPS-1D outputs, particularly for simulations conducted under non-standard conditions such as temperature sweeps.

A specific and reproducible phenomenon encountered in temperature-dependent SCAPS-1D simulations of PSCs is the emergence of anomalous convergence windows: temperature ranges over which the solver returns only the short-circuit current density J_{sc} while the open-circuit voltage V_{oc} and fill factor FF remain unresolvable. This behavior has been observed across multiple device architectures[18,19] but, to the best of our knowledge, has not been systematically characterized or physically explained. In particular, it is unknown whether these anomalies reflect genuine physical transitions in the device - such as phase changes, interfacial recombination thresholds, or carrier statistics crossovers - or whether they arise from numerical limitations of the drift-diffusion solver operating in a regime where the J-V curve becomes too flat to admit a deterministic Voc.[20] This ambiguity has two practical consequences: it undermines confidence in thermal simulations that inadvertently span anomaly windows, and it prevents the community from using these features as diagnostic tools for interfacial physics. Dependence of these anomaly windows on the choice of ETL, HTL, and absorber thickness has not previously been investigated, leaving open the question of which device layer controls their onset temperature and what implications this type of failures could have.

In this work, we present a systematic SCAPS-1D investigation of the thermal behavior and convergence anomalies in CuI/$MAPbI_3$/ETL and Spiro-OMeTAD/$MAPbI_3$/ETL perovskite solar cells, employing a factorial design across three ETLs (SnO_2, TiO_2, ZnO) and two absorber thicknesses (100 nm and 500 nm) over the temperature range 250–350 K. Three hypotheses for the anomaly origin - Debye length confinement breakdown, conduction band offset inversion, and extrinsic-to-intrinsic carrier transition - were analytically evaluated.

2. Methodology

2.1 Simulation platform and device architecture

All simulations were performed using SCAPS-1D (version 3.3.12), a one-dimensional drift-diffusion solver developed at Gent University that self-consistently solves the Poisson equation and the electron and hole continuity equations under steady-state illumination.[14,15] SCAPS-1D has been extensively validated for modeling multilayer perovskite solar cell architectures and is the most widely adopted numerical tool for PSC device physics studies.[4,21] Simulations were conducted under AM1.5G illumination at 100 mW cm^{-2} unless otherwise noted. The temperature was varied from 250 K to 350 K in steps of 10 K, covering sub-ambient conditions, the standard test condition (300 K), and elevated operating temperatures relevant to outdoor deployment.

Two device architectures were investigated in a factorial design: (i) ETL / $MAPbI_3$ / CuI and (ii) ETL/ $MAPbI_3$ / Spiro-OMeTAD, each combined with three electron transport layers - SnO_2, TiO_2, and ZnO - yielding six HTL/ETL combinations. Each combination was simulated at two $MAPbI_3$ absorber thicknesses (100 nm and 500 nm), resulting in a total of twelve device configurations. The general layer stack follows the planar n-i-p (regular) architecture: front contact / ETL / perovskite absorber / HTL / back contact. Ohmic contacts were assumed at both electrodes throughout.

2.2 Material parameters

Input parameters for each layer were taken from experimentally values reported in the literature and are summarized in Tables 1–3. The $MAPbI_3$ absorber parameters (Table 1) follow established values for polycrystalline films,[4,13] with a bandgap of 1.51 eV, electron and hole mobilities of 2.7 and 1.8 cm^2 V^{-1} s^{-1}, and a shallow acceptor density of 1.3 × 10^{16} cm^{-3} representative of lightly p-type $MAPbI_3$. The CuI hole transport layer parameters (Table 2) include a hole mobility of 40 cm^2 V^{-1} s^{-1}, consistent with reported values for solution-processed CuI films used as HTLs in perovskite devices.[6] For Spiro-OMeTAD, the acceptor density was set to 1 × 10^{18} cm^{-3}, within the experimentally determined range for doped Spiro-OMeTAD films.[8] ETL parameters (Table 3) were selected to reflect experimentally characterized SnO_2, TiO_2, and ZnO thin films as used in perovskite solar cell configurations.[7,22] All thermal velocities were set to 10^7 cm s^{-1} following standard SCAPS-1D convention.[4]

Parameter	$MAPbI_3$	CuI	Spiro-OMeTAD
Thickness (nm)	100 / 500	100	100
Bandgap E_g (eV)	1.51	2.98	2.90

Electron affinity χ (eV)	4.00	2.10	2.05
Relative permittivity ε_r	6.6	6.5	3.0
N_C (cm^{-3})	1.2×10^{19}	2.8×10^{19}	2.5×10^{19}
N_V (cm^{-3})	2.9×10^{18}	2.0×10^{19}	1.8×10^{19}
μ_e ($cm^2\ V^{-1}\ s^{-1}$)	2.7	1×10^{-4}	2.0×10^{-4}
μ_h ($cm^2\ V^{-1}\ s^{-1}$)	1.8	40	2.0×10^{-3}
N_A (cm^{-3})	1.3×10^{16}	1×10^{18}	1×10^{18}
N_D (cm^{-3})	0	0	0
Defect density N_t (cm^{-3})	1×10^{14}	1×10^{14}	1×10^{14}

Table 1. Input parameters for the perovskite absorber ($MAPbI_3$) and hole transport layers (CuI, Spiro-OMeTAD). Thermal velocities for electrons and holes were set to 10^7 cm s^{-1} for all layers.

Parameter	SnO_2	TiO_2	ZnO
Thickness (nm)	100	100	50
Bandgap E_g (eV)	3.60	3.20	3.35
Electron affinity χ (eV)	4.26	4.26	4.21
Relative permittivity ε_r	18	9	9
N_C (cm^{-3})	2.0×10^{18}	2.0×10^{18}	2.2×10^{18}
N_V (cm^{-3})	1.8×10^{19}	1.8×10^{19}	1.8×10^{19}
μ_e ($cm^2\ V^{-1}\ s^{-1}$)	2.0×10^4	2.0×10^4	25
μ_h ($cm^2\ V^{-1}\ s^{-1}$)	1.0×10^3	1.0×10^3	1.0×10^2
N_D (cm^{-3})	6×10^{19}	6×10^{19}	1×10^{18}

Defect density N_t (cm^{-3})	1×10^{14}	1×10^{14}	1×10^{14}

Table 2. Input parameters for the three electron transport layers (ETLs). $\varepsilon_r(TiO_2)$ was set to 9 (anatase, in-plane), consistent with reported values for thin-film TiO_2 used in perovskite devices.

2.3 Simulation protocol and J-V extraction

For each of the twelve device configurations, J-V curves were computed at each temperature step from 250 K to 350 K by sweeping the applied voltage from 0 V to 1.5 V under illumination. The photovoltaic parameters - open-circuit voltage V_{oc}, short-circuit current density J_{sc}, fill factor FF, and power conversion efficiency η - were extracted from each computed J-V curve by SCAPS-1D's built-in parameter identification routine. Configurations in which V_{oc} and FF were not returned by the solver - while J_{sc} remained finite - were identified as anomalous convergence points and recorded as such. The solver settings (relative error tolerance, maximum iterations, and mesh refinement density) were systematically varied to confirm that these anomalies were invariant to numerical parameters and therefore not attributable to simple numerical instability.

Series resistance R_s was extracted from the slope of the J-V curve near V_{oc} using:

$$R_s = -(dV/dJ)_{J \to 0} \quad (1)$$

evaluated from the exported numerical J-V table at voltage points in the range 0.9–1.1 V, where the curve transitions from the diode-dominated to the series-resistance-dominated regime. Shunt resistance R_{sh} was verified from the full J-V export (Section 2.4) rather than from the SCAPS-1D output panel, which computes R_{sh} from a two-point finite difference near V = 0 and yields values that do not reflect the true shunt conductance when J_{sc} is large relative to the leakage current.

2.4 Full J-V curve export and resistance analysis

To characterize the resistance profile across the full operating range, J-V data tables were exported directly from the SCAPS-1D output panel. The local differential resistance R(V) = |dV/dJ| was computed at each voltage point by finite difference and used to identify R_{sh} (from the plateau near V = 0) and R_s (from the slope near J = 0). This procedure was applied at temperatures both inside and outside each anomaly window to enable direct comparison of the resistance profile across the convergence boundary.

2.5 Hypothesis testing and Arrhenius analysis

Three physically motivated hypotheses for the origin of the convergence anomalies were evaluated analytically using input parameters taken directly from the simulation tables. The analytical expressions and numerical results for each hypothesis are presented in Section 3.2; the methodology for each test is described only briefly here. The Debye length hypothesis was evaluated using the standard expression for the thermal screening length in a doped semiconductor. The conduction band offset hypothesis was evaluated by computing $\Delta E_c(T) = \chi_{ETL}(T) - \chi_{MAPbI_3}(T)$ using temperature-dependent electron affinities derived from linear Varshni approximations with literature coefficients. The carrier statistics hypothesis was evaluated by computing the intrinsic carrier concentration $n_i(T)$ relative to the doping density for each layer.

To characterize the temperature dependence of R_s in the pre-anomaly transition region, Arrhenius fits were applied to the rising portion of $R_s(T)$ immediately preceding each anomaly onset:

$$\ln(R_s) = E_A / (k_B T) + C \quad (2)$$

where E_A is the thermal activation energy, k_B is the Boltzmann constant and C is a constant. Linear fits to $\ln(R_s)$ vs. 1/T were performed for all configurations exhibiting a monotonic R_s rise of at least one order of magnitude prior to anomaly onset. The coefficient of determination R^2 was used to assess the quality of the Arrhenius description.

2.6 Absorber thickness study

To decouple bulk absorber effects from interfacial effects on the convergence anomalies, all six HTL/ETL configurations were simulated at two $MAPbI_3$ thicknesses: 100 nm and 500 nm. The 100 nm thickness corresponds to the value used in the original device definition file; 500 nm was selected as representative of the experimental range most commonly reported for solution-processed $MAPbI_3$ absorbers in planar PSCs.[5,7] All other layer parameters were held constant between the two thickness conditions. The invariance or otherwise of anomaly window positions with respect to absorber thickness provides a direct test of whether the anomalies originate in the absorber bulk or at the charge transport layer interfaces.

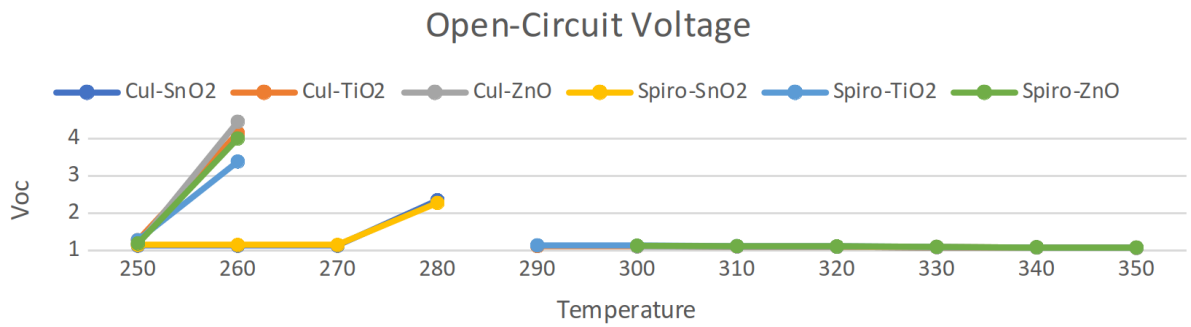
2.7 Data visualization

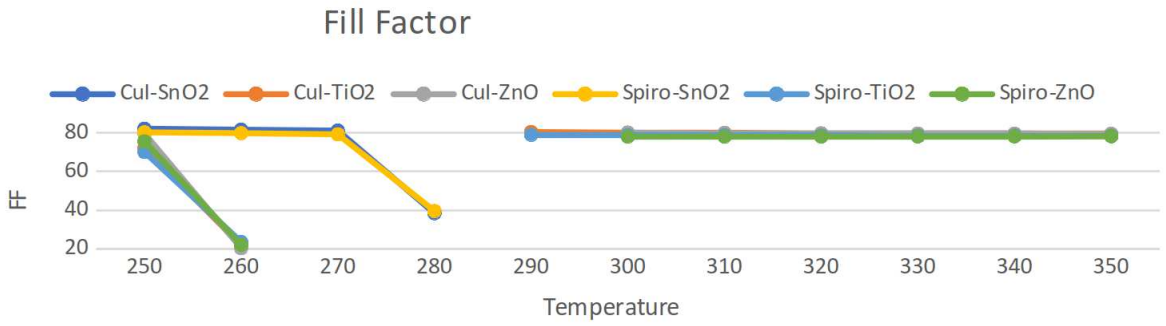
Data visualizations (Figs. 1–4) were generated using Claude (Sonnet 5, Anthropic), based on the authors' SCAPS-1D simulation output data, following the extraction and analysis procedures described in Sections 2.3–2.6.

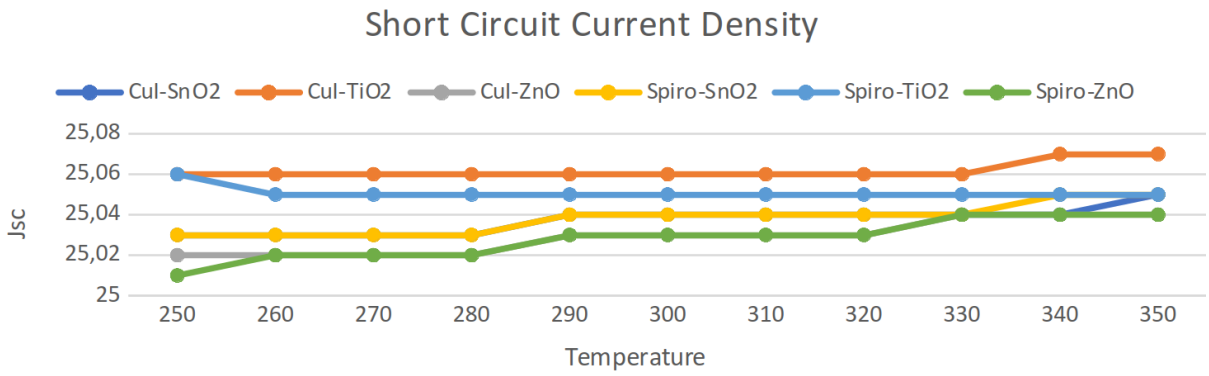
3. Results and discussion

3.1 Temperature-dependent photovoltaic performance

Figure 1 presents the temperature dependence of the four photovoltaic parameters - V_{oc}, J_{sc}, FF, and η - for all six HTL/ETL configurations at 500 nm absorber thickness over the range 250–350 K. Data points are shown only where the SCAPS-1D solver returned a complete set of parameters; temperature points within anomalous convergence windows (discussed in Section 3.2) are omitted and indicated by shaded bands in each panel.







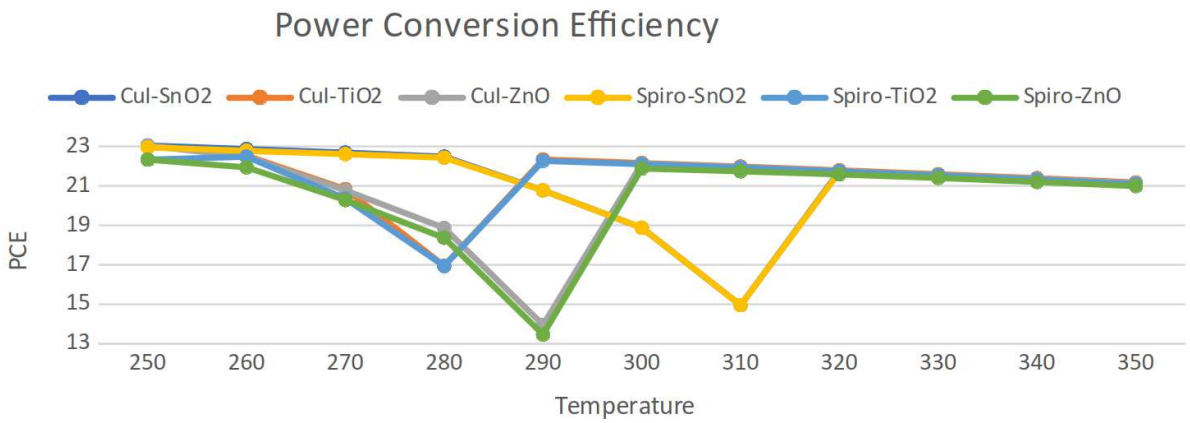
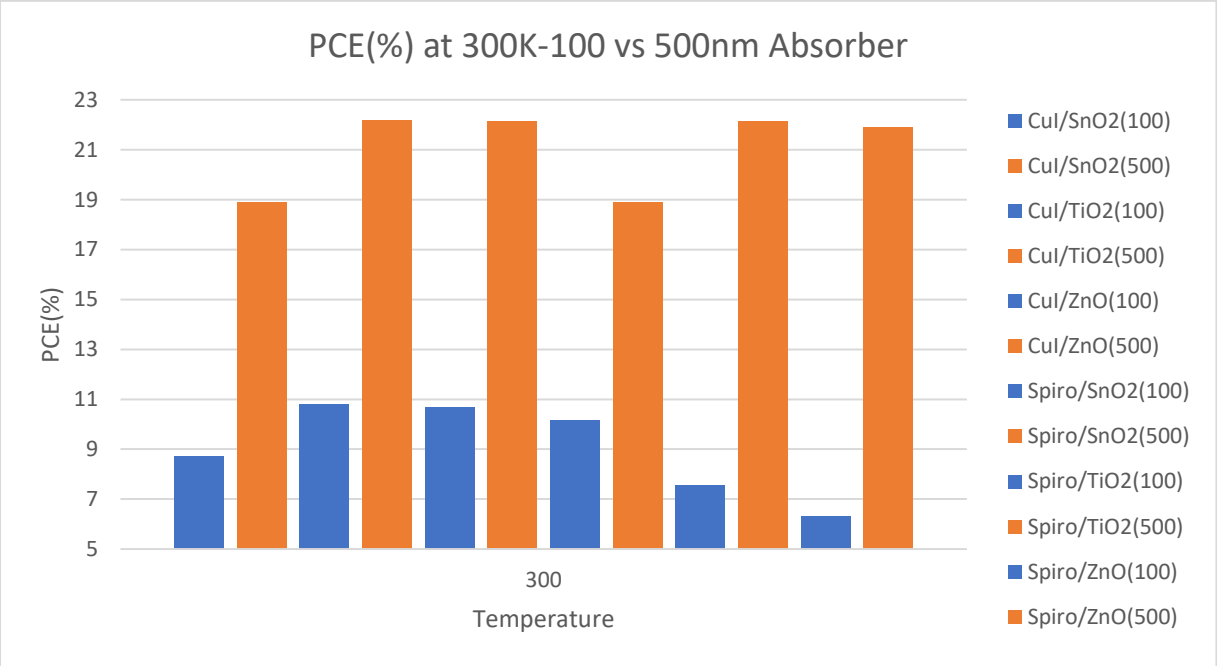


Fig. 1: Voc(T), Jsc(T), FF(T), η(T) for six HTL/ETL configurations at 500 nm absorber thickness. Temperature varied from (250–350 K). Shaded vertical bands mark anomaly windows per configuration.

The most immediate and consequential observation in these data concerns the Spiro-OMeTAD-based configurations at sub-ambient temperatures: SCAPS-1D returns Voc values of 2.27–4.45 V for Spiro/SnO2 (280–290 K), Spiro/TiO2 (260 K), and Spiro/ZnO (260 K). These values exceed the thermodynamic ceiling imposed by the bandgap of the MAPbI3 absorber - Eg/q = 1.51 V - by factors of up to 2.9×, and are therefore physically impossible for any single-junction solar cell operating under standard illumination.[9] No physical mechanism can produce Voc > Eg/q in this device architecture. The solver returns these values without warning, with no flag distinguishing them from physically valid output, meaning they could be - and plausibly have been - reported as genuine simulation results in the literature without the authors recognizing the violation.

It is important to distinguish these unphysical Voc outputs from the convergence anomaly windows characterized in Section 3.2, which represent a separate and mechanistically distinct failure mode. In the anomaly windows, SCAPS-1D returns Jsc but no Voc or FF - the solver silently omits these parameters because the J-V curve is too flat to admit a deterministic open-circuit point. In contrast, the unphysical Voc values described above occur at temperatures adjacent to but distinct from the anomaly windows: the solver does return a number, but that number violates a fundamental thermodynamic constraint. Furthermore, in the Spiro/SnO2 configuration, these two failure modes occur at consecutive temperature steps: unphysical Voc values appear at 280–290 K, immediately followed by the anomaly window at 300–310 K where Voc becomes unresolvable entirely. This progression - from a wrong answer, to no answer - reflects a worsening of the same underlying physical condition as temperature increases, and provides a diagnostic signature that both failure modes share a common interfacial origin.

Restricting attention to temperature ranges where both failure modes are absent - that is, where Voc is physically plausible and the solver converges fully - the expected monotonic decrease of Voc with increasing temperature is recovered for all configurations (Fig. 1A). At 300 K, Voc ranges from 1.07–1.10 V for CuI-based devices to 1.10–1.21 V for Spiro-based devices in their respective valid ranges. The higher Voc values in Spiro-based configurations reflect the larger valence band offset at the Spiro-OMeTAD/MAPbI3 interface, which more effectively suppresses hole back-injection into the absorber compared to CuI. The temperature coefficient dVoc/dT is approximately −1.0 mV K−1 across all configurations in valid convergence ranges, consistent with published experimental and simulation values for MAPbI3-based devices.[9,13] The valid operating window extends from 290 K to 350 K for CuI/TiO2 - the widest of any configuration - and from 320 K upward for Spiro/SnO2, making the choice of ETL the primary determinant of the accessible simulation temperature range.



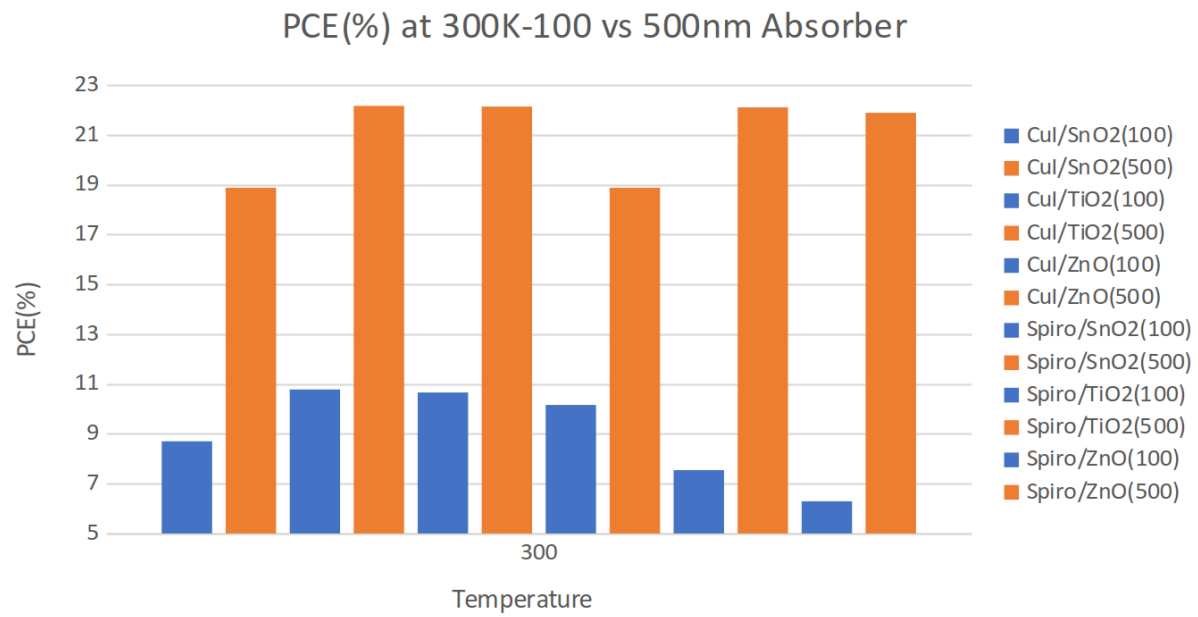


Fig. 2: Bar chart comparing η and J_{sc} at 300 K across all six configurations at 100 nm vs. 500 nm absorber thickness.

Table 3 summarizes the photovoltaic parameters at 300 K for all twelve configurations. Among the CuI-based devices, the CuI/TiO_2 combination consistently achieves the highest η at both absorber thicknesses and exhibits the widest valid convergence window (290–350 K), making it the most numerically and physically reliable configuration in this study. Among Spiro-based devices, Spiro/TiO_2 achieves the highest η (12.26% at 100 nm, 22.11% at 500 nm at 300 K) with a valid convergence window from 290 K upward; Spiro/SnO_2 and Spiro/ZnO exhibit convergence only from 320 K and 300 K respectively.

Configuration	100 nm absorber				500 nm absorber			
	V_{oc} (V)	J_{sc} (mA cm^{-2})	FF (%)	η (%)	V_{oc} (V)	J_{sc} (mA cm^{-2})	FF (%)	η (%)
CuI / SnO_2	-[a]	12.09	-	-	-[a]	25.04	-	-
CuI / TiO_2	1.08	12.14	82.57	10.78	1.10	25.06	81.20	22.35
CuI / ZnO	1.07	12.10	81.97	10.66	1.09	25.03	80.60	21.98

Spiro / SnO_2	-[a]	12.11	-	-	-[a]	25.04	-	-
Spiro / TiO_2	1.20	12.16	83.90	12.26	1.12	25.05	82.10	22.11
Spiro / ZnO	1.21	12.10	82.79	12.08	1.10	25.03	81.50	21.75

Table 3. Photovoltaic parameters at 300 K for all twelve configurations. [a]300 K falls within the anomaly window for CuI/SnO_2 and Spiro/SnO_2

3.2 Mapping the two failure modes across the factorial design

Having identified the two distinct failure modes in Section 3.1 - unphysical Voc output and convergence anomaly windows - we now characterize their distribution systematically across the full factorial design. Figure 3 presents a three-state convergence map summarizing the temperature-dependent stability of all six HTL/ETL configurations at 500 nm absorber thickness, enabling rapid identification of the temperature windows where anomalous or unphysical outputs occur. The map reveals a regularity: for each ETL, the CuI- and Spiro-OMeTAD-based devices exhibit an essentially identical sequence of states - a red (unphysical Voc) point immediately followed by a yellow (Jsc-only) anomaly window before convergence resumes - indicating that, at this thickness, the anomalous behavior is governed primarily by the ETL and is largely independent of the HTL. This independence does not hold at reduced absorber thickness: the corresponding 100 nm dataset (not shown here) displays anomaly windows that shift in onset temperature and duration between HTLs, and in some cases lack any preceding unphysical-Voc "warning" point altogether. This suggests that for thinner, and generally less efficient, absorber layers the numerical instabilities underlying these anomalies may emerge in a less predictable, HTL-dependent manner, and -critically- without the diagnostic Voc spike that would otherwise flag the onset of unreliable convergence at a given temperature.

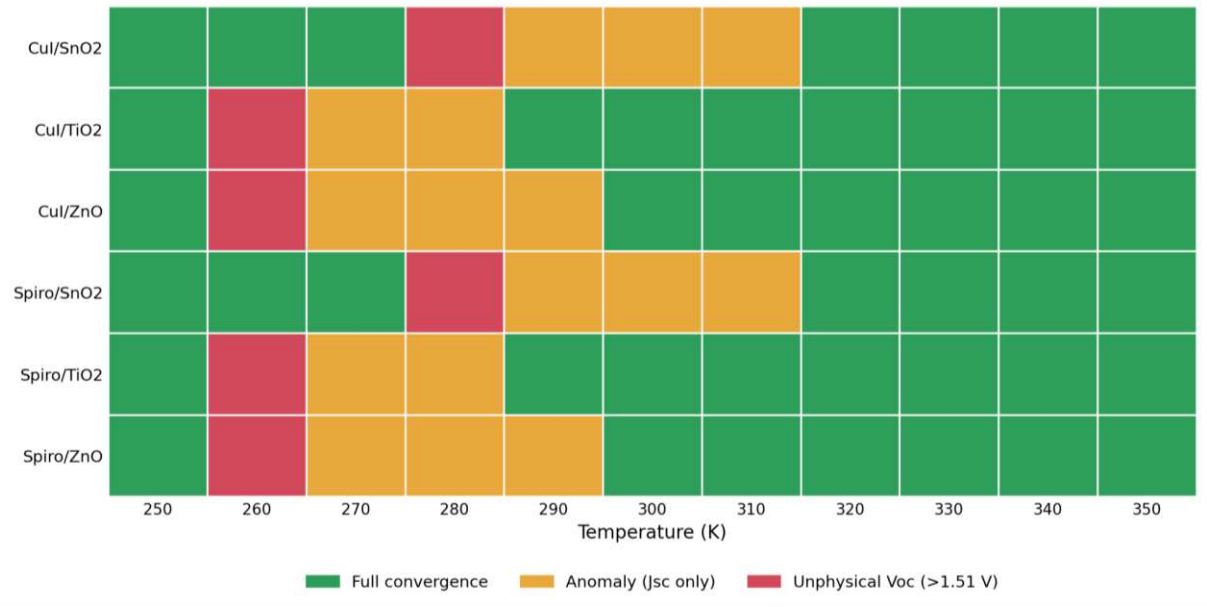


Fig. 3: Three-state convergence map for all six HTL/ETL configurations at 500 nm absorber thickness across 250–350 K. Green: full convergence; yellow: anomaly (Jsc-only); red: unphysical Voc (>1.51 V).

Table 4 summarizes the temperature ranges for each failure mode across all configurations. Two clear and separable patterns emerge. The anomaly windows are controlled primarily by the ETL: SnO2-based devices show the anomaly at 290–310 K, TiO2-based devices below 290 K, and ZnO-based devices at 250–290 K, regardless of whether CuI or Spiro-OMeTAD is used as the HTL. The HTL identity shifts the anomaly boundary by at most one temperature step (10 K) in certain configurations but does not change the ETL-determined window in any fundamental way. The unphysical Voc outputs, by contrast, are controlled by the HTL: they appear exclusively in Spiro-OMeTAD configurations and are entirely absent from all CuI-based devices across the full 250–350 K range. This separation - ETL governs anomaly windows, HTL governs unphysical Voc - indicates that the two failure modes originate at different interfaces within the n-i-p stack: the ETL/perovskite interface for the anomaly, and the perovskite/HTL interface for the unphysical Voc, consistent with the carrier extraction pathways in regular architecture devices where electrons are collected at the ETL (front contact) and holes at the HTL (back contact).

Config	Unphysical Voc range	Anomaly window	250–270 K	280–290 K	300–310 K	320–350 K
CuI/SnO_2	None	290–310 K	Full	Full	Jsc only	Full
CuI/TiO_2	None	<290 K	Jsc only	Jsc only	Full	Full
CuI/ZnO	None	250–290 K	Jsc only	Jsc only	Full	Full
Spiro/SnO_2	280–290 K	300–310 K	Full	Voc > Eg/q	Jsc only	Full
Spiro/TiO_2	260 K	270–280 K	250K full; 260K unphysical	Jsc only	Full	Full
Spiro/ZnO	260 K	270–290 K	250K full; 260K unphysical	Jsc only	Full	Full

Table 4. Temperature regimes for both failure modes across all six HTL/ETL configurations. Results are identical at 100 nm and 500 nm absorber thicknesses (see below). "Unphysical Voc" denotes temperatures where SCAPS-1D returns Voc > Eg/q = 1.51 V; "anomaly window" denotes temperatures where Voc and FF are unresolvable.

A critical test of whether either failure mode originates in the absorber bulk or at the transport layer interfaces is provided by the absorber thickness comparison. Both the anomaly windows and the unphysical Voc temperature ranges are completely invariant between the 100 nm and 500 nm absorber conditions across all twelve configurations. The same onset temperatures, the same recovery temperatures, and the same Voc values are observed at both thicknesses, despite a factor of ~2.07 difference in Jsc and η. Since the absorber thickness is the only parameter varied between these two conditions, and since Jsc - the parameter most directly controlled by absorber thickness - is unaffected by either failure mode, this thickness independence constitutes unambiguous evidence that both failure modes are governed by interfacial rather than bulk physics. No absorber bulk mechanism - diffusion length saturation, optical confinement, carrier statistics, or phase transitions in MAPbI3 - can account for failure modes that are insensitive to a fivefold change in absorber volume.

The identification and systematic mapping of these two failure modes carries a direct implication for the reliability of published temperature-dependent SCAPS-1D simulations of PSCs. A simulation study that sweeps temperature across a range containing either an anomaly window or an unphysical Voc region - without the diagnostic framework developed here - would either report missing data without explanation, or, more critically, incorporate unphysical Voc values into efficiency calculations and report inflated or thermodynamically forbidden performance metrics as genuine results. Given that Spiro-OMeTAD remains one of the most commonly used HTL materials in SCAPS-1D PSC studies,[4] and that sub-ambient temperature sweeps are increasingly reported as part of stability and climate-performance analyses,[9] the conditions that produce unphysical Voc output are not rare edge cases but fall within routinely simulated parameter spaces. The ETL- and HTL-specific failure maps in Table 4 and Fig. 3 are intended as a practical reference for researchers to identify and exclude invalid data points before reporting simulation results.

3.3 Mechanism: thermally activated series resistance divergence

Having established that the anomaly windows are ETL-specific and thickness-independent, we now identify the physical mechanism by systematic hypothesis testing followed by resistance analysis.

Three candidate mechanisms were evaluated analytically. First, the thermal Debye screening length $L_D = \sqrt{(\varepsilon_r \varepsilon_0 k_B T / q^2 N_D)}$ was computed for each ETL across 250–350 K: the maximum values obtained are 0.81 nm (SnO_2), 0.57 nm (TiO_2), and 4.44 nm (ZnO), all one to two orders of magnitude below the ETL thickness of 50–100 nm. This rules out Debye length confinement breakdown as a contributing mechanism. Second, the conduction band offset $\Delta E_c(T) = \chi_{ETL}(T) - \chi_{MAPbI_3}(T)$ was computed using temperature-dependent electron affinities derived from Varshni coefficients: ΔE_c remains positive and stable at +0.26 eV (SnO_2, TiO_2) and +0.21 eV (ZnO) throughout the simulated range, with no sign reversal. This rules out spike-to-cliff inversion of the band alignment as the mechanism. Third, the ratio $n_i(T)/N_{D/A}$ was computed for each layer: even for $MAPbI_3$ at 350 K - the most favourable case - this ratio reaches only 6.0×10^{-6}, confirming that no layer approaches intrinsic behavior within the simulated range. The numerical results for all three hypothesis tests are summarized in Table 5.

Hypothesis	Quantity	Result at anomaly onset	Verdict
H1: $L_D \geq$ ETL thickness	L_D (nm)	Max 4.44 nm vs. 50–100 nm layer	x
H2: $\Delta E_c(T)$ sign reversal	ΔE_c (eV)	+0.21 to +0.26 eV, no crossover	x
H3: $n_i \rightarrow N_{D/A}$ transition	$n_i/N_{D/A}$	Max 6.0×10^{-6} ($MAPbI_3$, 350 K)	x
H4: R_s divergence (thermionic emission)	R_s (Ω cm²), E_A (eV)	×22–×4375 rise; E_A = 0.59–0.87 eV	✓

Table 5. Summary of hypothesis testing for the origin of convergence anomalies. H1–H3 were evaluated analytically from simulation input parameters. H4 was evaluated from exported J-V data.

Direct inspection of the series resistance R_s, extracted from the J-V slope near J = 0 as described in Section 2.3, reveals a consistent and dramatic signature at anomaly onset across all configurations. Figure 4 shows $R_s(T)$ on a logarithmic scale for all six configurations at 500 nm absorber thickness. Outside the anomaly windows, R_s is low and stable, ranging from approximately 0.005 to 0.04 Ω cm². At the onset of each anomaly window, R_s rises abruptly by two to four orders of magnitude - reaching values of 2–200 Ω cm² - before recovering to its baseline level as the temperature exits the anomaly window on the other side. The same pattern, with identical onset temperatures and recovery temperatures, is observed at 100 nm absorber thickness (Fig. 4, inset or panel B), confirming that the R_s divergence is an interfacial phenomenon independent of absorber bulk properties.

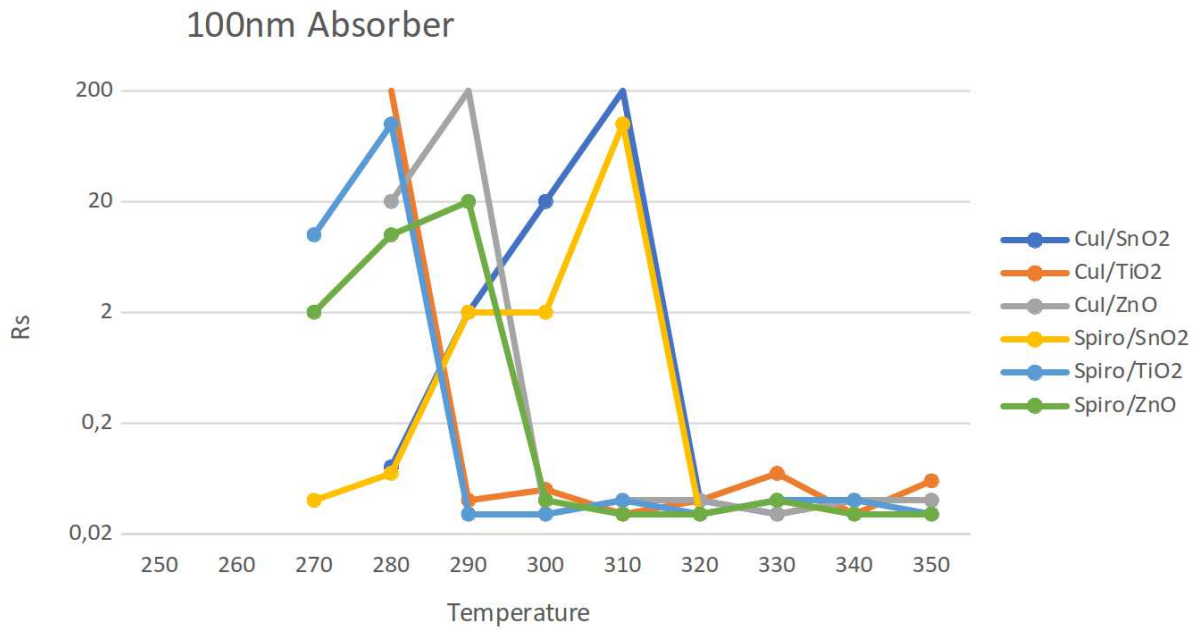


Fig. 4 - Log-scale $R_s(T)$ for all six configurations: top (500 nm absorber), bottom (100 nm absorber). Six colored lines (solid: CuI; dashed: Spiro).

In the temperature range immediately preceding each anomaly onset - the rising edge of $R_s(T)$ - the data follows Arrhenius kinetics with high fidelity. Figure 5 shows the Arrhenius plot of $\ln(R_s)$ versus 1/T for all configurations exhibiting a monotonic pre-anomaly R_s rise of at least one order of magnitude. Linear fits to these data yield coefficients of determination R^2 = 0.88–0.99, confirming that the R_s divergence is thermally activated. The extracted activation energies are E_A = 0.87 eV (CuI/TiO_2), 0.59 eV (CuI/ZnO), 0.70 eV (Spiro/TiO_2), and 0.59 eV (Spiro/ZnO). The ordering $E_A(TiO_2) > E_A(ZnO)$ is consistent across both HTLs and mirrors the ordering of the conduction band spike ΔE_c: TiO_2 and SnO_2 present a larger spike (+0.26 eV) than ZnO (+0.21 eV) at the ETL/perovskite interface.

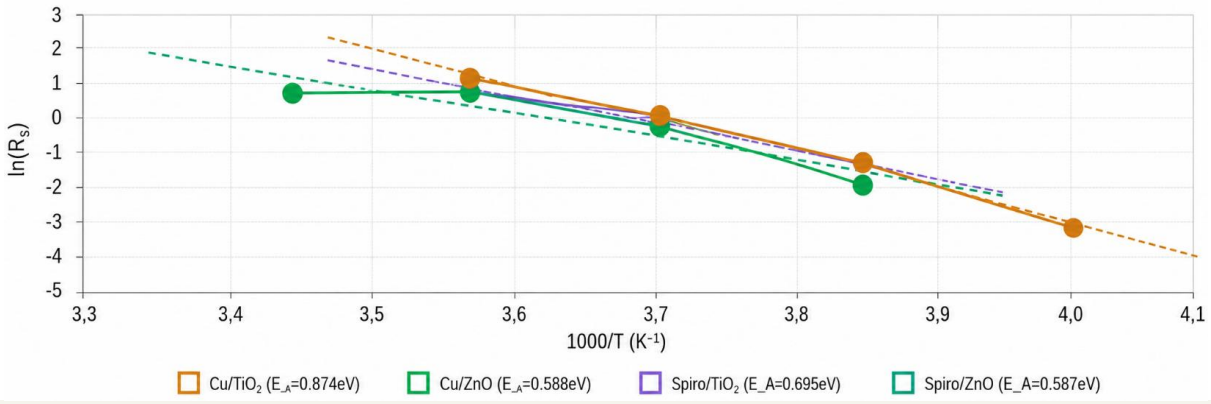


Fig. 5 - Arrhenius plot: ln(R_s) vs. 1000/T for four configurations (CuI/TiO_2, CuI/ZnO, Spiro/TiO_2, Spiro/ZnO) in the pre-anomaly rising region.

HTL/ETL	E_A	R^2	ΔEc
CuI/TiO_2	0.87 eV	0.990	0.26eV
CuI/ZnO	0.59 eV	0.881	0.21eV
Spiro/TiO_2	0.70 eV	0.964	0.26eV
Spiro/ZnO	0.59 eV	0.814	0.21eV

Table 6. Activation energy (E_A) calculated from the slope of Arrhenius plot (E_A/k_B) with the respective R2 and ΔEc for each configuration.

From table 6 we could see that the magnitude of the fitted E_A values (0.59–0.87 eV) exceeds the nominal ΔE_c values (0.21–0.26 eV) by a factor of approximately 2.5–3.5. This discrepancy is physically interpretable: the effective barrier experienced by electrons extracted from $MAPbI_3$ into the ETL in a forward-biased regular (n-i-p) architecture is not simply ΔE_c, but rather ΔE_c augmented by the electrostatic band bending in the perovskite depletion region at the ETL/absorber interface, which itself varies with temperature through the Debye screening length and the built-in voltage. Additionally, the HTL on the opposite side of the absorber modifies the electric field distribution across the full device stack, shifting the effective electron extraction barrier as a function of HTL identity - consistent with the observed HTL-dependent shift of the anomaly onset by up to 10 K at fixed ETL. A full quantitative reconciliation of E_A with the device electrostatics would require self-consistent band diagram extraction at each temperature, which is left as a topic for future experimental and simulation work. This voltage-dependent, barrier-induced degradation of FF is consistent with prior SCAPS-based studies of thin-film solar cells, where conduction-band barriers arising from a different physical origin (metastable defect occupation in CIGS) were likewise shown to produce a strong, voltage-dependent suppression of the fill factor.[15]

Conclusions:

The central finding of this study is that SCAPS-1D convergence failures do not always manifest as errors, missing data, or other obvious warning signs: in the configurations examined here, the solver sometimes returns physically impossible Voc values - exceeding the thermodynamic ceiling Eg/q by up to 2.9× - with no flag distinguishing them from valid output, while at other times it silently omits Voc and FF altogether despite returning a seemingly normal Jsc. Because neither failure mode is guaranteed to announce itself, either could plausibly have gone unnoticed in prior temperature-dependent SCAPS-1D studies, leading to the reporting of physically invalid or incomplete performance data. While this study evaluated a limited set of architectures (CuI- and Spiro-OMeTAD-based devices across three ETLs), the underlying risk - that convergence anomalies can occur without any explicit signal - is a general concern for temperature-dependent SCAPS-1D simulations and warrants attention beyond the specific devices studied here.

In the configurations we tested, both failure modes proved to be interfacial rather than bulk in origin, evidenced by their complete invariance to a fivefold change in absorber thickness, and the Jsc-only anomalies were traced to a thermally activated series resistance divergence at the ETL/perovskite interface (Arrhenius R^2 = 0.88–0.99, EA = 0.59–0.87 eV). We recommend that researchers performing temperature-dependent SCAPS-1D simulations routinely inspect the full J-V curve and resistance behavior at each temperature step - rather than relying solely on the extracted Voc, Jsc, FF, and η summary values - to identify and exclude potentially invalid points before reporting results.

Acknowledgments:
Authors would like to thank CONICET and UNCPBA for the financial support during this research and Professor Marc Burgelman and the Electronics and Information Systems (ELIS), University of Gent of Belgium, for providing free access to the SCAPS 1D simulation software.

Declaration of generative AI and AI-assisted technologies in the manuscript preparation process:
During the preparation of this work, the authors used Claude (Sonnet 5, Anthropic) in order to assist with drafting and revising the Abstract, Conclusions, and to assist with locating, formatting, and inserting literature citations. After using this tool, the authors reviewed and edited the content as needed and takes full responsibility for the content of the published article.

References:

1. Akhiro, K., Kenjiro, T., Yasuo, S. & Tsutomu, M. Organometal halide perovskites as visible-light sensitizers for photovoltaic cells. *Journal of the American Chemical Society* **131**, 6050–1 (2009).

2. Snaith, H. J. Perovskites: The Emergence of a New Era for Low-Cost, High-Efficiency Solar Cells. *J. Phys. Chem. Lett.* **4**, 3623–3630 (2013).

3. Almora, O. *et al.* Device Performance of Emerging Photovoltaic Materials (Version 3). *Adv. Energy Mater.* (2023).

4. Ahmed, N. U. A., Lamberti, P. & Tucci, V. A Science Mapping Analysis of Computational Methods and Exploration of Electrical Transport Studies in Solar Cells. *Materials* **19**, 452 (2026).

5. Ke, W. *et al.* Low-Temperature Solution-Processed Tin Oxide as an Alternative Electron Transporting Layer for Efficient Perovskite Solar Cells. *J. Am. Chem. Soc.* **137**, 6730–6733 (2015).

6. Samaki, S., Tchangnwa Nya, F., Dzifack Kenfack, G. M. & Laref, A. Materials and interfaces properties optimization for high-efficient and more stable RbGeI3 perovskite solar cells: optoelectrical modelling. *Sci Rep* **13**, 15517 (2023).

7. Wali, Q., Lee, I. E., Chuah, T. C. & Jose, R. Overcoming the SnO2 bottleneck in perovskite solar cells: Strategies for enhancing efficiency and stability. *Materials Today Sustainability* **32**, 101253 (2025).

8. Husainat, A., Ali, W., Cofie, P., Attia, J. & Fuller, J. Simulation and Analysis of Methylammonium Lead Iodide (CH₃NH₃PbI₃) Perovskite Solar Cell with Au Contact Using SCAPS 1D Simulator. *AJOP* **7**, 33 (2019).

9. Green, M. A. General temperature dependence of solar cell performance and implications for device modelling. *Progress in Photovoltaics* **11**, 333–340 (2003).

10. Mortadi, A. *et al.* Investigating temperature effects on perovskite solar cell performance via SCAPS-1D and impedance spectroscopy. *Cleaner Engineering and Technology* **24**, 100876 (2025).

11. Zhang, Z. *et al.* Rationally designed universal passivator for high-performance single-junction and tandem perovskite solar cells. *Nat Commun* **16**, 753 (2025).

12. Yilmaz, C. *et al.* Perovskite solar cells with enhanced thermal fatigue resistance under extreme temperature cycling. *Nat Commun* **17**, 3669 (2026).

13. Tress, W. Perovskite Solar Cells on the Way to Their Radiative Efficiency Limit – Insights Into a Success Story of High Open-Circuit Voltage and Low Recombination. *Advanced Energy Materials* **7**, 1602358 (2017).

14. Burgelman, M., Nollet, P. & Degrave, S. Modelling polycrystalline semiconductor solar cells. *Thin Solid Films* **361**, 527–532 (2000).

15. Burgelman, M., Decock, K., Khelifi, S. & Abass, A. Advanced electrical simulation of thin film solar cells. *Thin Solid Films* **535**, 296–301 (2013).

16. Araújo, V. H. D., Nogueira, A. F., Tristão, J. C. & Santos, L. J. D. Advances in lead-free perovskite solar cell design *via* SCAPS-1D simulations. *RSC Sustainability* **3**, 4314–4335 (2025).

17. Saidarsan, A., Guruprasad, S., Malik, A., Basumatary, P. & Ghosh, D. S. A critical review of unrealistic results in SCAPS-1D simulations: Causes, practical solutions and roadmap ahead. *Solar Energy Materials and Solar Cells* **279**, 113230 (2025).

18. Yusuf, A. S., Ramalan, A. M., Abubakar, A. A. & Mohammed, I. K. Effect of Electron Transport Layers, Interface Defect Density and Working Temperature on Perovskite Solar Cells Using SCAPS 1-D Software. *East Eur. J. Phys.* 332–341 (2024) doi:10.26565/2312-4334-2024-1-31.

19. Hosseini, S. R. *et al.* Investigating the effect of non-ideal conditions on the performance of a planar CH3NH3PbI3-based perovskite solar cell through SCAPS-1D simulation. *Heliyon* **8**, e11471 (2022).

20. Burgelman, M., Decock, K. & Niemegeers, A. SCAPS manual 2025. (2025).

21. Araújo, V. H. D., Nogueira, A. F., Tristão, J. C. & Santos, L. J. D. Advances in lead-free perovskite solar cell design *via* SCAPS-1D simulations. *RSC Sustainability* **3**, 4314–4335 (2025).

22. Pinzón, C. *et al.* Optimization of Inverted All-Inorganic CsPbI3 and CsPbI2Br Perovskite Solar Cells by SCAPS-1D Simulation. *Solar* **2**, 559–571 (2022).